Bericht des Instituts für Aerodynamik und Strömungstechnik
Report of the Institute of Aerodynamics and Flow Technology

IB 124-2009/9

Calculations of Shock-Boundary Layer Interaction for a Supersonic Ramp Flow by DNS, Using a Fourth order Finite Difference Method

H. Lüdeke, N.D. Sandham

Herausgeber:
Deutsches Zentrum für Luft- und Raumfahrt e.V.
Institut für Aerodynamik und Strömungstechnik
Lilienthalplatz 7, Germany, 38108 Braunschweig

ISSN 1614-7790

Stufe der Zugänglichkeit: 1
Braunschweig, im Dezember 2009

Institutsdirektor:
Prof. Dr.-Ing. habil. C.-C. Rossow

Verfasser:
Dr.-Ing. H. Lüdeke
Prof. N.D. Sandham

Abteilung: Raumfahrt
Abteilungsleiter:
Dr.-Ing. J.M.A. Longo

Der Bericht enthält:
35 Seiten
22 Bilder
1 Tabelle
24 Literaturstellen

Abstract

Despite intensive theoretical and experimental research, transition to turbulence in separated hypersonic ramp flows is still a challenge to predict. One of the most successful approaches to model the dominant mechanisms is the direct numerical simulation approach, which has demonstrated, despite the well known drawback of computationally costly simulations, the capability to generate reliable datasets. To allow calculations of the transition process on ramp configurations a validated DNS code with high resolution of the turbulent structures in the hypersonic flow regime is a necessity. The abilities of the 4^{th}-order finite-difference version of the DLR FLOWer code, derived originally for Large Eddy Simulations (LES) over recent years is a promising choice for the requested properties. In fact, it was shown in former studies that the resolution of transitional instabilities in supersonic boundary layers is very well within the range of this code. In the present study, different supersonic test cases are chosen from literature and compared with the actual simulations using this high-order version of the DLR FLOWer code. The results using higher-order Pade-filter approaches are encouraging. With this validation as a background, a supersonic ramp-test case was chosen for study. To resolve the transition process, different ramp-angles and Reynolds numbers were investigated to determine a transitional test case, for which turbulence can be resolved behind re-attachment. A hypersonic ramp with 12° angle of attack at a moderate Reynolds number was then chosen for three-dimensional DNS calculations of the transition process. These DNS were carried out with various grid densities and grid extents in the wall-normal and spanwise direction with good success. The investigation of different spanwise extents of the simulation region has demonstrated the capabilities of the code to predict the supersonic transition process.

Contents

1 Introduction

A typical phenomenon in trans, super- and hypersonic flows is the shock/boundary-layer interaction (SBLI) in the separated area of a hypersonic ramp-flow. The phenomenon can result in reduced performance (e.g. in engine inlets), increased drag (e.g. on airfoils and other aerodynamic surfaces) and, especially in the hypersonic case, increased surface heating. Consequently, these flow phenomena have been investigated extensively, for a variety of geometric configurations and over a broad range of Mach- and Reynolds numbers. Several reviews of the work have been published for example by Adamson and Messiter [1], Delery [2], Dolling [3] and Knight et al. [4]. As shown by simulation results of Pagella and Rist [5], the typical two-dimensional SBLI flow-field can be mapped onto a hypersonic ramp flow with the half incidence angle as the ramp angle β. In principle, if the spanwise extent of the ramp is wide enough, the resultant flow field will be essentially two-dimensional (2D) in nature.

If the pressure gradient over the ramp is sufficiently strong, the boundary layer will separate in front of the hinge line and reattach downstream, forming a closed separation bubble with a separation shock in front of the bubble.

While many previous studies on hypersonic ramps have been concerned with fully developed turbulent boundary layers, a significant and challenging aspect is the influence of boundary-layer transition throughout the separation bubble. Boundary-layer transition itself is a process that, despite extensive study over many years, is not yet fully understood. It is generally accepted that, at a sufficiently high Reynolds number, disturbances inherent in the flow or created by some external means, become unstable and provoke transition from laminar to turbulent flow in the boundary layer. However, in addition to the Reynolds number, many other factors influence this process also, including the level of acoustic freestream turbulence, wall roughness, wall temperature, and the Mach number of the flow (see Saric et al. [6] Ma and Zhong [7]). Results from linear stability analysis (LSA) of compressible flows are reported in detail in Mack [8] for attached boundary layers. At low Mach numbers ($Ma < 0.3$), the Tollmien Schlichting (first mode) waves are the most unstable disturbances beyond a critical Reynolds number. As the Mach number increases, additional Mack-modes (second mode, third mode, etc.) of instability appear, and at high Mach numbers these are the most unstable disturbances [9]. Flow stability results in SBLI at M = 4.8, focusing on the second-mode instabilities, are reported in Pagella et al. [5] for a flat plate boundary layer and at M = 5.373 in Balakumar et al. [10] for a compression corner flow.

The parabolized stability equations (PSE; see Herbert Hein et al. [11]) approach improves on the e^n method (Arnal and Casalis [12] Stock [13]) by including nonparallel terms and allowing for the streamwise evolution of disturbance shape functions. The

method is applicable to convectively unstable flow but, although widely used for transition prediction on wings, it does not appear to have been extensively applied to SBLI until now. Direct numerical simulation (DNS) has been applied extensively to study transition in low-speed flows (e.g., Kleiser and Zang [14]) and a few applications have been made to SBLI flows.

Pagella et al. [5] created a 2D SBLI by impinging an oblique shock wave on a flat plate boundary layer at a Mach number of 4.8. In this work, the response of the initially laminar boundary layer to artificially introduced small amplitude disturbances was investigated and the results agreed well with those of linear stability theory. This work was later extended to the case of a 2D compression ramp flow, also at Mach 4.8 (Pagella et al. [5]), showing that, when the impinging shock and the shock created by the compression ramp have the same strength, the characteristics of SBLI and ramp flow were identical, validating the so-called free interaction concept originated by Chapman et al. [15]. This latter work also demonstrated that the response to small-amplitude disturbances was practically identical.

Compression corner flows at M1 = 5.373 were also considered by Balakumar et al. [10] who showed that the second-mode disturbances were not significantly amplified over the separation bubble. In a later study of the same compression corner flow, Zhao and Balakumar [16] showed that a (0 , 2) mode arising from nonlinear interactions led to an oblique type of breakdown.

Nonlinear disturbances and breakdown to turbulence in a flat plate boundary layer with an impinging shock were considered by Teramoto [17] using large-eddy simulation at Mach 2.0. At a high pressure ratio (p3/p1 = 1.91), it was found that transition occurred even at zero free-stream turbulence level. This indicates the presence of absolute instability of the laminar base flow, although the resolutions used were not sufficient to achieve grid-independent results.

In the present study, the case of a hypersonic compression ramp at different ramp angles and Reynolds-numbers is investigated. Like Pagella et al. [5] a two-dimensional test case at M=4.8 and a high inflow Reynolds number is investigated and compared with the literature results. Aside from grid resolution studies different ramp angles and Reynolds number are taken into account to choose appropriate flow conditions for a transitional test case for DNS simulations. Due to the large number of parameters influencing the flow field, only selected ones are varied, while an adiabatic wall temperature as a boundary condition was kept for all test cases.

For the three-dimensional (3D) simulations white noise forcing in the beginning of the calculation-cycle was imposed as a perturbation, such that the unstable modes could emerge naturally without additional inflow perturbations and to investigate the convective or absolute character of the instability under the given flow conditions.

After carrying out a number of 2D supersonic code validation cases, discussing the simulations in comparison with literature data, results of 2D simulations of the undisturbed ramp-flow are presented and compared with literature-data from Pagella and Rist [5]. This ramp result was taken as a starting point for varying ramp-angle and Reynolds number as influencing parameters for the size and stability of the separation zone. From the results, appropriate flow conditions and the extent of the computational domain was chosen for subsequent three-dimensional DNS simulations.

Finally, 3D Navier-Stokes simulations using random finite-amplitude disturbances are described. These were carried out to demonstrate the feasibility of the early-stage nonlinear breakdown and transition onset over the separation bubble.

2 Numerical tools

Two 4^{th}-order finite difference codes are used in this work for the simulation of different test cases. On the one hand the well validated DNS solver of the University of Southampton, which is called the SBLI code in the following, on the other the finite-difference version of the DLR-FLOWer code which is well validated for industrial applications in it's second-order finite volume formulation, but has been used recently for DNS cases in the scope of transition control by ultrasonic absorptive surfaces (see [9]).

2.1 The DLR Flower-code

The equations to be solved are the compressible Navier-Stokes equations for flow of a perfect gas with density ρ, velocity components u_i, pressure p and internal energy e, written in conservation law form as:

$$\frac{\partial \rho}{\partial t} + \frac{\partial \rho u_j}{\partial x_j} = 0 \tag{2.1}$$

$$\frac{\partial \rho u_i}{\partial t} + \frac{\partial \rho u_i u_j}{\partial x_j} + \frac{\partial p}{\partial x_i} = \frac{\partial \tau_{ij}}{\partial x_j} \tag{2.2}$$

$$\frac{\partial \rho E}{\partial t} + \frac{\partial (\rho E + p) u_i}{\partial x_i} = -\frac{\partial q_i}{\partial x_i} + \frac{\partial u_i \tau_{ij}}{\partial x_j}, \tag{2.3}$$

where $E = e + u_i u_i/2$. The equations are closed with the perfect gas law:

$$p = \rho R T, \tag{2.4}$$

where R is the gas constant, together with the constitutive relations:

$$q_i = -\kappa \frac{\partial T}{\partial x_i} \tag{2.5}$$

and

$$\tau_{ij} = \mu \left(\frac{\partial u_i}{\partial x_j} + \frac{\partial u_j}{\partial x_i} - \frac{2}{3} \delta_{ij} \frac{\partial u_k}{\partial x_k} \right). \tag{2.6}$$

The base flow is obtained from a separate solution of the similarity equations for compressible boundary layer flow, solved by a shooting method. For all calculations perfect gas is considered at a Prandtl number of Pr $= 0.72$ and a ratio of specific heats

$\gamma = 1.4$. Viscosity μ is prescribed by Sutherland's law with a constant of 110.4K and a reference temperature of T_∞. The same Sutherland coefficients are used for the thermal conductivity κ. The wall-normal co-ordinate of the prescribed inflow profile for the ramp-flow is normalized by the displacement thickness before being interpolated onto the simulation grid by a cubic spline method.

Calculations in this paper were made with a 4^{th}-order variant of the DLR FLOWer code. The basic FLOWer code solves the compressible Reynolds-averaged Navier Stokes equations on block-structured grids with second-order finite volume techniques and cell-centred or cell vertex variables. The high-order version used in the present work [18] uses 4^{th}-order central differencing based on standard compact finite differences in a cell-centred formulation, together with high-order compact filters that are applied at the end of each time step. Options are available for a skew-symmetric splitting the convective terms and for sponge-zone boundary conditions to reduce reflections. For the present work we use a 6^{th}-order filter and the standard conservative form of the Euler terms. Time advancement is obtained by a five-step second-order Runge Kutta method [19]. To calculate non-trivial geometries a transformation of the curvilinear co-ordinates onto cartesian, equidistant simulation grids is carried out by the use of transformation matrices and metric-terms [20]. This technique is used in the following for the calculation of supersonic ramp-flows.

The calculations use periodic boundary conditions in z direction for the ramp-flow calculations and also in x direction for the validation test-cases. A no-slip wall with temperature set to the wall temperature of the base flow is applied at $y = 0$. At the outer boundaries characteristic conditions including a sponge-layer are used and at the outflow a zero-gradient condition is prescribed.

For the sponge-layer Boundary condition a source-term Q is added on the right hand side of the Navier-Stokes equations (see [20]). This is shown in the following for the continuity equation:

$$\frac{\partial \rho}{\partial t} + \frac{\partial \rho u_j}{\partial x_j} = Q \tag{2.7}$$

with:

$$Q = \sigma(x)(\rho - \rho_{ref}) \tag{2.8}$$

where ρ_{ref} is the density at the farfield boundary and σ is defined locally by:

$$\sigma(x) = \sigma_0 \left(\frac{d}{D_{max}} \right)^{\beta}. \tag{2.9}$$

Here d is the distance from the farfield, D_{max} is the maximum-thickness of the sponge-layer and β is an exponent to force the influence of the sponge-layer source-term. The default values for these parameters are $\beta = 2.0$ and $\sigma_0 = 2.0$. For the transformation into curve-linear co-ordinates the source-term as well as the equations are multiplied by the determinant of the Jacobean. For the momentum and energy equations the source-term is defined in the same way.

The implicit filtering in the field (see [21]) is defined by:

$$\alpha_F \tilde{f}_{i+1} + \tilde{f}_i + \alpha_F \tilde{f}_{i-1} = \sum_{n=0}^{N} \frac{\alpha_n}{2} (f_{i+n} + f_{i-n}) \tag{2.10}$$

where $\tilde{f}_i$ is the filtered quantity of f_i. α_F is a free parameter for influencing the damping of the filter within the range of:

$$-0.5 < \alpha_F < 0.5 \tag{2.11}$$

With increasing filtering order $2 \cdot N$ and and increasing α_F the filter dissipation decreases. The standard value, used for α_F is 0.4 in the following. At the boundaries one-sided filters are used for as many points as necessary to introduce the filter of the prescribed order by using a separate boundary-filter parameter. The transfer functions for different filter parameters and orders are investigated in detail by S. Enk in [20].

For the oblique-shock test case an unsteady 4^{th}-order inflow condition was implemented to generate the periodic perturbations, described in the next section.

2.2 The Southampton SBLI-code

The SBLI code of the University of Southampton is a widely used DNS solver of the compressible Navier Stokes equations, with a 4^{th}-order non-compact finite difference formulation. A wide range of parameters allows high resolution shock capturing near discontinuities without losing the higher-order properties in turbulent regions. For this reason it is used for cross-validations of the supersonic-ramp test case with the DLR FLOWer code, using identical grids, boundary conditions and numerical treatment, including the 6^{th}-order filtering of the results.

3 Investigated flow configurations and test cases

3.1 Supersonic vortex pairing

As proposed by Yee and Sandham [22], different compressible test-cases with grid refinement studies were simulated to validate the code for the final DNS simulations. The case of supersonic vortex pairing is intended to study the vortex growth and pairing in a temporal mixing layer at a convective Mach number of 0.8. For these conditions shock waves are generated by perturbations from the vortices, and consequently the challenge for this test case is to calculate an accurate and highly resolved vortex-flowfield for a minimum number of grid points while in addition limiting oscillations around the shocks. A detailed description of this case, including grid studies can be found in [22]. The initial flow field is defined as:

$$u = 0.5 \ \tanh(2y) \tag{3.1}$$

with the velocity normalized by the velocity jump $u_1 - u_2$ across the shear layer while all coordinates are normalized by the vorticity thickness:

$$\delta_w = \frac{u_1 - u_2}{(du/dy)_{max}}. \tag{3.2}$$

The subscripts 1 and 2 refer to the upper and lower part of the flowfield with positive and negative inflow velocity respectively. Both fluid streams have the same density and temperature for upper- and lower boundary and the Reynolds number, defined by the velocity jump, vorticity thickness and kinematic viscosity of the fluid is set to be 1000. Sutherlands law with a reference temperature of 300K is used to calculate local viscosities from the temperature.

To provide a defined temporal behaviour of the evolving shear layer, disturbances are defined using a Fourier expansion with only two contributing terms:

$$v' = \sum_{k=1}^{2} a_k \cos(2\pi k x / L_x + \phi_k) \exp(-y^2/b) \tag{3.3}$$

with L_x as the box length in x-direction and $b = 10$ as the y-modulation. The pairing is simulated by this definitions in the center of the computational domain by choosing

the initially most unstable wave $k = 2$ with an amplitude of $a_2 = 0.05$ and a phase of $\phi_2 = -\pi/2$. The subharmonic wave $k = 1$ is defined by $a_1 = 0.01$ and $\phi_1 = -\pi/2$. The defined perturbations correspond approximately to the eigenfunctions of the linear stability analysis (see [22]) for the compressible mixing layer and provide a well defined start instability that evolves quickly and can be easily compared with data from other groups.

All Grids for the two-dimensional Cartesian test cases are generated by the well known mapping:

$$y = \frac{L_y}{2} \frac{\sinh(b_y \eta)}{b_y} \tag{3.4}$$

In this equation $L_y = 100$ is the domain-size in y-direction. A stretching factor of $b_y = 3.4$ was taken from the literature and η is an equally spaced co-ordinate perpendicular to the flow-direction, running from -1 to +1.

The non-dimensional time step of the FLOWer code uses a scaling factor of $\sqrt{RT_\infty}/L_{ref}$ while the factor in the literature is chosen with $2 \cdot u_\infty/L_{ref}$. Consequently a conversion factor for comparison of the time-scales is necessary which can be determined as $2 \cdot Ma\sqrt{\gamma}$ by comparing the dimensional time. For the present test case this conversion factor is 1.893, between FLOWer- and literature data.

For the boundary conditions periodicity is expected for x_{min} and x_{max} condition, while slip conditions are set at upper and lower boundaries.

Two grid refinement studies at point-numbers of 101x101 and 201x201 were carried out with 2^{nd}- and 4^{th}-order schemes to demonstrate the capabilities of the different approaches.

3.2 Oblique shock wave with impinging mixing-layer

The second test case is set up to investigate the behaviour of the schemes by resolving the shock wave interacting with vortices of an unstable, spacially evolving shear layer. For this purpose an oblique shock is generated at the inflow at an initial convective Mach number of 0.6. The shear layer vortices have to pass through this shock and the successive one, reflected from the lower solid wall. The flow field was set up in such a way, that the flow is supersonic everywhere at the outflow which simplifies the boundary treatment in this part and allows a direct insight into the behaviour of the scheme instead of the boundary conditions.

As already mentioned an oblique shock from the upper corner of the inflow impacts the shear layer. By this interaction a deflected shock wave below and expansion waves above the shear layer are generated. For simplicity and comparability with results from literature [22] the lower boundary is chosen as a slip condition to allow shock reflection without shock-boundary layer interaction.

Quantity	Upper stream Inflow	Lower stream Inflow	Upper stream after shock
u-velocity	3.0000	2.0000	2.9709
v-velocity	0.0000	0.0000	-0.1367
Θ (deg)	0.0000	0.0000	2.6343
density	1.6374	0.3626	2.1101
pressure	0.3327	0.3327	0.4754
sound speed	0.5333	1.1333	0.5616
Mach number	5.6250	1.7647	5.2956

Table 3.1: Flow conditions at the boundaries for the oblique-shock, shear-layer interaction test case.

As well as in the former section, the inflow is chosen as a tanh-profile, but with an offset of 2.5:

$$u = 2.5 + 0.5 \ \tanh(2y) \tag{3.5}$$

By this definition a shear layer is defined with velocities of $u_1 = 3$ above and $u_2 = 2$ below the layer. The convective Mach number is naturally defined by:

$$M_c = \frac{u_1 - u_2}{c_1 + c_2} \tag{3.6}$$

with c_1 and c_2 as free-stream sound speeds in the respective region, equal to 0.6. Pressure and stagnation temperature above- and below the shear-layer are expected to be equal for the initial conditions.

The flow properties at the boundaries from [22] are given in Table 3.1 and set up a shock a the upper inflow-corner with a 12° angle. A unit Reynolds number of 500 was chosen for this test.

To set up a defined instability of the shear layer, again fluctuations are added in a similar way as for the last case:

$$v' = \sum_{k=1}^{2} a_k \cos(2\pi k t/T + \phi_k) \exp(-y^2/b) \tag{3.7}$$

This definition results in a transient inflow-condition, dependent on the period $T = \lambda/u_c$ with the wavelength $\lambda = 30$ and the parameters: $b = 10$, $a_1 = a_2 = 0.05$ and $\phi_2 = \pi/2$ without a phase shift for $k = 1$. Perturbations are only added to the v-component as a convenient start-up procedure as described in the literature.

As well as in the former test-case the grid is uniform in streamwise direction and refined in y-direction in the shear layer region, following equation (3.4) from the last section with $b_y = 1$. Since the shear-layer spreads further for this test and is additionally deflected by the shock, the stretching is chosen much lower, than for the vortex-pairing grid. Grid dimensions are defined as $L_x = 200$ and $L_y = 40$.

3.3 Laminar ramp flow

This two-dimensional ramp is chosen as a test-case for direct numerical simulations of supersonic separated ramp configurations. The detailed investigations of Pagella and Rist [5] are chosen to validate the code results against a highly resolved data-base. An advantage of this case is the laminar character of the flow which was on the other hand shown to be unstable to small perturbations. To save computational effort a laminar inflow profile was generated at a certain position upstream of the separation position and kept over the whole calculation. This profile was generated externally by a shooting method under the assumption of parallel flow [9]. It consequently does not fit entirely to the incoming flat-plate boundary layer which is growing, but provides a sufficient well defined inflow condition that only generates a weak shock without a strong impact on the separation region. The conditions at inflow are taken from [5] and [23] as $M = 4.8$, $T_\infty = 55.4$ and T_{wall} is adiabatic. The global Reynolds number Re_L of 100000 based on an internal length scale L was then rescaled on the displacement thickness of the boundary layer at inflow δ_{in}, which was used as a reference length for the reported calculations. The procedure to obtain this inflow Reynolds number $Re_{\delta,in}$ will be described in the following for a comprehensive overview. To define the position of the inflow plane, the local Reynolds number is defined by the streamwise co-ordinate x and the global Reynolds number Re_L

$$R_x = \sqrt{x/L\, Re_L} \tag{3.8}$$

The inflow Reynolds number $Re_{\delta,in}$, based on the displacement thickness at inflow, is provided in [23] for an $R_x = 1100$ as $Re_{\delta,in} = 12546$. Since flow field data was provided in front of this position and also for further calculations with larger separation regions an inflow plane upstream of this position was chosen at $R_x = 600$. The corresponding $Re_{\delta,in} = 6843.3$ is calculated by using the linear relation between displacement thickness and R_x. In the following only the generic value of $Re_{\delta,in} = 6843$ will be used. The spatial scaling of the following calculation is based entirely on the displacement thickness, so the x-position of the inflow plane had to be calculated by using equation (3.8) for the x-coordinate scaled with L and the ratio of L and δ_{in} as a scaling factor:

$$\frac{L}{\delta_{in}} = \frac{Re_L}{Re_{\delta,in}}. \tag{3.9}$$

For comparisons with literature data the co-ordinates will be re-scaled.

The boundary conditions for this test case were a constant inflow-profile at $x = x_{min}$ as described, a sponge layer far-field condition of 12 points at $y = y_{max}$ for the source-term influence to prevent shock-reflection and finally at $x = x_{max}$ a zero-gradient outflow condition. The grids for the ramp configuration are generated using the same $\sinh$-distribution in the wall normal direction, described in the previous sections. This time a stretching factor $b_y = 3.5$ was chosen to resolve the boundary layer. This Cartesian grid was then transformed into a smooth ramp grid by using a conformal mapping of the original grid [24].

For the start-up procedure of the three-dimensional DNS calculation the two-dimensional solution was distributed on the spanwise staggered grid and a random

perturbation was added to the smooth laminar base-flow. The procedure will be described in detail in the following sections. Different grid densities were investigated for the two- and three-dimensional test cases between 601x169 points for a number of single-block simulations up to 1153x185 grid points for the set-up of the DNS with grid resolutions up to 1153x185x64 points.

4 Results

4.1 Simulation of supersonic vortex pairing

The transient behaviour of the vortex-pairing test case, taken from [22], is shown in Figure 1, calculated by the 4^{th}-order finite difference scheme on the 201x201 point grid which is the finest one and consequently taken as a reference solution. As an implicit filtering a 6^{th}-order Pade filter with 4^{th}-order treatment at the domain-boundaries was chosen at a standard filter-parameter $\alpha_{flt} = 0.4$, which provides good smoothing properties as well as low influence on the spectral behaviour of the scheme (see [20]). The resulting temperature contours are shown at four subsequent time steps, chosen in a way to be comparable with the literature data. In comparison with the results of Yee and Sandham [22] very good agreement for all time instants could be achieved. The shear-layer starts to roll up in the first stage, while first shocks are developed in the second and starts a strong interaction of the pairing vortices appears in the third. In the final figure of the row a very detailed shock- and vortex pattern is apparent between the interacting structures, which is still a challenge to resolve with a reasonably coarse grid resolution.

The same results are shown for a second-order AUSMDV scheme, without any further filtering or acceleration techniques in Figure 2. The resulting shocks are slightly better resolved and the field is less noisy behind the shock-waves. On the other hand the resolution at the final stage is also less pronounced, but still allows a resolution of the relevant features.

In the following a comparison of the last stage of vortex-pairing at different grid densities will be shown for the different schemes, filtered by different techniques. This is demonstrated for the described schemes and the coarse- and fine grid with 101x101 and 201x201 grid points respectively in Figure 3. The superior resolution of the 4^{th}-order scheme is visible by comparing the results with the coarse grids, where the resolution of the AUSMDV scheme is obviously strongly reduced.

This is an encouraging first validation result to show the capabilities of the finite difference approach, using higher-order filtering even for shock-dominated flows, as long as the strength of the shocks does not exceed a certain limit.

4.2 Simulation of an oblique-shock shear-layer interaction

For the following test case the inflow Mach-number is considerably stronger, taking into account the inflow-condition up to Mach 5.6 as shown in Table 3.1.

For this case the density distribution is shown in Figure 4, using a comparable convective timestep as given by the literature [22], transformed into the reference system of the FLOWer code. After hitting the shear layer, the shock is deflected in the lower part of the flow field and interacts a second time with the developed shear layer vortices after the shock-reflection at the lower boundary. The first interaction zone results in a deflection of the shear layer while the second one produces a rich pattern of shocks and shocklets, which has to be resolved by the scheme.

In Figure 4 the resolution of the Pade scheme for a 641x161 grid is shown in the upper part while the simulation in the lower part was carried out on the coarse grid with 321x81 points. Again the fine-grid solution is expected as a reference to be compared with the other ones. As expected the resolution of the weaker shocks is better for the results on a fine grid, while the coarse-grid solution still includes all relevant flow features, especially in the vortex-region.

The situation is different for the second-order version of the code (see Figure 5). While the fine-grid solution on top still includes all shocks and vortex structures, the lower resolution decreases the vortex-resolution in a way, that only the basic flow features remain. This is in good agreement with the investigations from literature [22], where the capabilities of second-, fourth and additionally sixth-order schemes were compared, obtaining the same results.

As a conclusion the capabilities of the 4^{th}-order finite difference scheme with higher-order Pade filtering in resolving unsteady supersonic flow features for a reasonable grid resolution without wasting computational effort were demonstrated conclusively, in good agreement with literature data of well validated DNS-schemes.

4.3 Results of two-dimensional laminar ramp flow

The calculations for the laminar ramp flow at Ma=4.8 were carried out by the local time stepping scheme of the FLOWer code to obtain steady results and by a global time stepping for the Southampton SBLI code. For both cases approximately 100000 iterations were necessary to get the final extent of the separation bubble which is growing slowly in terms of a typical CFD calculation effort. Different extents of the grids in wall normal direction were tested to show the influence of the far-field boundary opposite to the wall and the related sponge-layer, the best results were obtained when the separation shock is kept below the $y = y_{max}$-boundary, leaving the calculation domain at the outflow boundary. Examples for the two-dimensional grids are shown in Figure 6 for 6° and 8° ramps with every 10^{th} grid point shown. For two-dimensional calculations, where the calculation effort was moderate such a grid was used for both FLOWer and SBLI simulations, while for the time consuming DNS calculations the wall-normal grid-extent was narrowed and a slight farfield-influence on the calcula-

tion was accepted. The calculations from the FLOWer- and SBLI code were carried out by using largely the same boundary conditions and higher-order implicit filtering to stabilize the 4^{th}-order numerical schemes used in both codes.

The density field including the streamlines in the separation region is shown in Figure 7 for the FLOWer code in comparison with results from the SBLI code of the University of Southampton and the reference solution from literature. Coordinates are rescaled after post-processing to obtain comparable scales. All results are in good agreement for the density distribution as well as the separation- and re-attachment position.

The direct comparison of the wall shear stress distribution in Figure 8 shows very good overall agreement between the two codes and the literature results for different grid-extents, steady and unsteady calculations as well as different filter parameters used in FLOWer. A slight deviation of the separation- and re-attachment point of about one grid cell between FLOWer- and SBLI code is visible, which could be a result of the cell-centered discretization in Flower in contrast to the cell-vertex discretization in the SBLI-code. Velocity profiles upstream the separation position at $R_x = 1000$, inside the separation bubble at $R_x = 1350$, and after re-attachment at $R_x = 1700$ are presented in Figure 9. The agreement of the profiles even inside the separation region shows the expected comparability of the different solvers. Finally a comparison of the wall-pressure is shown in Figure 10. Since the inflow profile was not an exact Navier-Stokes solution, a weak shock was generated behind the inflow point, visible on the pressure profiles at $R_x = 600$. To compare the data with the literature results, the pressure behind this shock, expected at $R_x = 680$, was taken as a reference for both codes and resulted in a good agreement, also for the wall pressure distribution. The deviations in the outflow region result from the zero-gradient boundary condition which is a standard approach for this kind of flows and will be expected to be sufficient in the following.

For all comparisons the FLOWer and SBLI-results were generally in better agreement with each other than with the literature data since identical grids and inflow profiles as well as numerical schemes and parameters were used for both calculations. As a consequence the laminar two-dimensional results can be expected as a converged solution of the supersonic ramp-flow.

In a next step the ramp-geometry and flow conditions for a sufficiently unstable separation bubble had to be found to get a start solution for the subsequent DNS calculations. Due to the large number of parameters involved in the problem, only the ramp angle and Reynolds-number based on the inflow-displacement-thickness were varied. The inflow profile was kept constant for all parameter variations. As expected the separation increases with increasing ramp angle. Density fields and streamtraces for $Re_{\delta,in} = 6843$ are shown in Figure 11 for ramp angles of $6°$, $8°$, $10°$ and $12°$. From $10°$ ramp angle secondary re-circulation zones appear which are much more pronounced for $12°$. All investigated cases show steady solutions for the local time stepping scheme. Variations of the inflow Reynolds number are shown in Figure 12-13. The separation decreases visibly with a decreasing $Re_{\delta,in}$, which can be understood by a smaller shear stress in the inflow region, which is easier to overcome by the inverse pressure gradient. This statement is confirmed by the c_f distribution at different ramp angles and Reynolds-numbers. While for a ramp-angle variation (Figure 14) the shear stress distribution behind the inflow is identical for all curves, it is reduced with

the Reynolds number at constant ramp angle, shown in Figure 15 by the c_f distribution over the x-co-ordinate. This results in the observed earlier separation and later re-attachment. The influence of the additional separation vortices is clearly visible by the additional zeros in c_f for the higher Reynolds numbers.

Due to the necessary grid-resolution for the successive DNS calculation, a moderate Reynolds number was chosen to allow large turbulent structures after transition to be resolved by the grid. Since one purpose of this study is to show the abilities of the code in DNS, the computational effort had to be kept moderate, and an extensive resolution of very fine turbulent structures has to be avoided in this stage. However the re-attachment region has to be sufficiently unstable to generate turbulence without damping out the imposed perturbations. Keeping these restrictions in mind, the largest simulated ramp-angle of 12° at a moderate $Re_{\delta,in} = 3422$ was chosen for the follow-on 3D calculations.

4.4 Direct numerical simulation of transition downstream ramp-separation region

To start the 3D calculations on a spanwise extruded grid of the 12° ramp configuration at $Re_{\delta,in} = 3422$, the steady 2D results were spanwise extruded onto the 3D grid. This steady flow field is perturbed by a white noise of 0.7% in all flow variables except for the spanwise velocity component which is set 10 times smaller than the noise in the wall-normal component. The last amplitude was chosen to get an initial mixing in spanwise direction but due to a strong amplification of this component in later calculation-stages not to force it too strongly. For each grid block a new random initial value was taken, determined by the grid block number, which leads to a deterministic random distribution as startup-perturbation in the whole field. Without any further interference the progress of this flow and the respective perturbations were investigated. The time step for the calculations was chosen by using a global time stepping scheme and estimating a sufficiently small time step.

For the spanwise extent of the computational grid it is necessary to resolve the smallest and largest order wavelengths by the cell size on the one hand and by the domain extent on the other. For the total spanwise extent about 1/12 of the separation length was chosen a minimal dimension, subdivided into 64 cells for the resolution of turbulent structures. The respective maximum streamwise x^+ and spanwise z^+ for this resolution was found in the range of $x^+_{max} \approx 20$ and $z^+_{max} \approx 15$ in the turbulent region after re-attachment. For all simulations the development of turbulent structures in the re-attachment region was observed, including the appearance of various shocks and shocklets. These discontinuities in the solution are a challenge for the numerical scheme, especially during the transition process in the re-attachment region. For this reason the time step has to be reduced significantly until the turbulence is fully developed. The resolution of the turbulent structures in this final stage is shown by the spanwise vorticity component in Figure 16-17 for three successive time instants, where Figure 17 is just a detail of the turbulent area. the visible turbulent region is moving downstream in time, so a convective nature of the instabilities, responsible for

the turbulence can be deduced. The turbulence is obviously not self-sustaining, consequently further simulations with sustained upstream turbulence will be necessary in future studies to investigate the transition process conclusively.

The resolution of the shocks and shocklets, generated by the turbulent boundary layer is visualized by density and pressure distributions in Figure 18-19 including the entropy as an additional quantity. Again Figure 19 is a detailed view of the turbulent part in the flow. In Figure 20 the impact of the turbulent boundary layer on the wall shear stress is shown at four time instants. Again the downstream movement of the turbulent region is clearly visible. The same calculation has been carried out on a spanwise doubled grid with the same initialization. The resulting wall shear stress is shown in Figure 21, with the same tendencies described for the former calculations.

To give an impression of the calculated three-dimensional structures, the spatial distribution of the vorticity, coloured by the spanwise velocity component is shown in Figure 22. The initial stage of the turbulent area is visibly dominated by streamwise vortex structures of a typical Görtler type.

5 Conclusion

The capabilities of the higher-order finite-difference version of the FLOWer-code have been evaluated in the present study by calculating a number of relevant supersonic test cases in comparison with literature results and standard upwind schemes. Furthermore, comparisons with a validated compressible DNS-code of similar kind were carried out using identical grids and inflow conditions, obtaining nearly identical results. Standard two-dimensional benchmark calculations from literature were chosen to show the capabilities in terms of shock- and vortex resolution of the different implemented schemes for different grid resolutions. Good results were obtained for the 4^{th}-order finite difference scheme, using 6^{th}-order implicit Pade filtering. Highly resolved vortex-interaction calculations, including shock and shocklet generation have shown the superior quality of this scheme for lower grid resolutions in comparison with a second-order AUSMDV scheme. This was confirmed by another unsteady test case of an oblique shock, interacting with an unstable shear layer and the resulting vortex structures. The capabilities of this scheme in terms of vortex resolution and shock treatment for Mach-numbers up to 5.6 were demonstrated successfully. After this validation the challenging test case of a separated supersonic ramp flow was chosen to show the DNS capabilities of the code for transition in the re-attachment region of these standard configurations. For comparison with existing data, the laminar calculations of Pagella and Rist [5] were re-calculated as a two-dimensional ramp-geometry. After successful comparison of Flower-results with this literature data and results of the Southampton-SBLI code, the ramp-angle and Reynolds-number of the case were varied to find a sufficiently unstable test case for DNS calculations. These calculations, with white noise as a start-up perturbation of the flow field, have shown the amplification of turbulence in the re-attachment region of the separation bubble and the movement of this generated turbulent region downstream. A technique to set up these configurations for different ramp geometries and grid densities was developed. The results were discussed and validated by the use of different ramp angles, grid densities and spanwise extents.

Bibliography

[1] Adamson, T. and Messiter, A., "Analysis of two-dimensional interactions between shock waves and boundary layers," *Anu.Rev.Fluid Mech.* **12**, 103, 1980.

[2] Delery, J., "Shock phenomena in high speed aerodynamics: still a source of major concern," *Aeronaut. J.* **1**, 19, 1999.

[3] Dolling, D., "Fifty years of shock-wave/boundary-layer interaction research: what next¿' *AIAA. J.* **39**, 1517, 2001.

[4] Knight, D., Yan, H., Panaras, A.G. and Zheltovodov, A., "Advances in CFD prediction of shock wave turbulent boundary layer interactions," *Prog. Aerospace. Sci.* **39**, 121, 2003.

[5] Pagella, A., Babucke, A. and Rist, U., "Two-dimensional numerical investigations of small-amplitude disturbances in a boundary layer at Ma=4.8: Compression corner versus impinging shock wave," *Physics of Fluids* **16** 7, 2272-2281, 2004.

[6] Saric, W.S., Reed, H.L. and White, E.B., "Stability and transition of three-dimensional boundary layers," *Annu. Rev. Fluid Mech.* **35**, 413, 2003.

[7] Ma, Y.B. and Zhong, X.L., "Receptivity of a supersonic boundary layer over a flat plate. Part 3. Effects of different types of free-stream disturbances," *J. Fluid Mech.* **532**, 63, 2005.

[8] Mack, L.,"Remarks on disputed numerical results in compressible boundary-layer stability theory," *Phys. Fluids* **27**, 342, 1984.

[9] Sandham, N.D. and Lüdeke, H., "A numerical study of Mach 6 boundary layer stabilization by means of a porous surface," *AIAA Journal*, textbf47, 2243, 2009.

[10] Balakumar, P., Zhao, H.W. and Atkins, H.,"Stability of hypersonic boundary layers over a compression corner," *AIAA J.* **43**, 760, 2005.

[11] Hein, S., Stolte, A. and Dallmann, U.C., "Identification and analysis of nonlinear transition scenarios using NOLOT/PSE," *Z. Angew. Math.*, textbf79, 109, 1999.

[12] Arnal, D., Casalis, C.,"Laminar turbulent transition prediction in three-dimensional flows," *Prog. Aerosp. Sci.* **36**, 173, 2000.

[13] Stock, H.W., "e(N) transition prediction in three-dimensional boundary layers on inclined prolate spheroids," *AIAA J.* **44**, 108, 2006.

[14] Kleiser, L. and Zhang, T.A., "Numerical simulation of transition in wall-bounded shear flows," *Annu. Rev. Fluid Mech.* **23**, 495, 1991.

[15] Chapman, D.R., Kuehn, D.M. and Larson, K.H., "Investigation of separated flows in supersonic and subsonic streams with emphasis on the effect of transition," *NACA Report* 1356, 1958.

[16] Zhao, H.W. and Balakumar, P.,"Nonlinear disturbance evolution across a hypersonic compression corner," *AIAA J.* **43**, 1034, 2005.

[17] Teramoto, S.,"Large-eddy simulation of transitional boundary layers with impinging shock wave," *AIAA J.* **43**, 2354, 2005.

[18] Enk, S., "A Fourth Order Finite Difference Method for Large Eddy Simulation at a Flat Plate," 16. DGLR-Fach-Symposium der STAB, November 3-4, 2008, Aachen, Germany.

[19] Kroll, N., Jain, R.K., "Solution of Two-Dimensional Euler Equations- Experience with a Finite Volume Code," DFVLR Forschungsbericht 87-41, (1987).

[20] Enk, S., "Ein Verfahren höherer Ordnung in FLOWer für LES,", DLR IB-124-2007/8, Institut für Aerodynamik und Strömungstechnik, Braunschweig, Germany 2007.

[21] Lele, S., "Compact finite differencing schemes with spectral like resolution,", Journal of computational physics, 103: 16-42, 1992.

[22] Yee, H.C., Sandham, N.D. and Djomehri, M.J., "Low-dissipative high-order shock-capturing methods using characteristic-based filters," *J. Comput Phys.* **150**, 199, 1999.

[23] Pagella, A., Rist, U. and Wagner, S., "Numerical invsetigations of small-amplitude disturbances in a boundary layer with impinging shock wave at Ma=4.8" *Physics of Fluids* **14** 7, 2088-2098, 2002.

[24] Lüdeke, H., "Untersuchung von Längswirbeln in abgelösten hypersonischen Strömungen," *DLR FB.* , 2003.

Figures

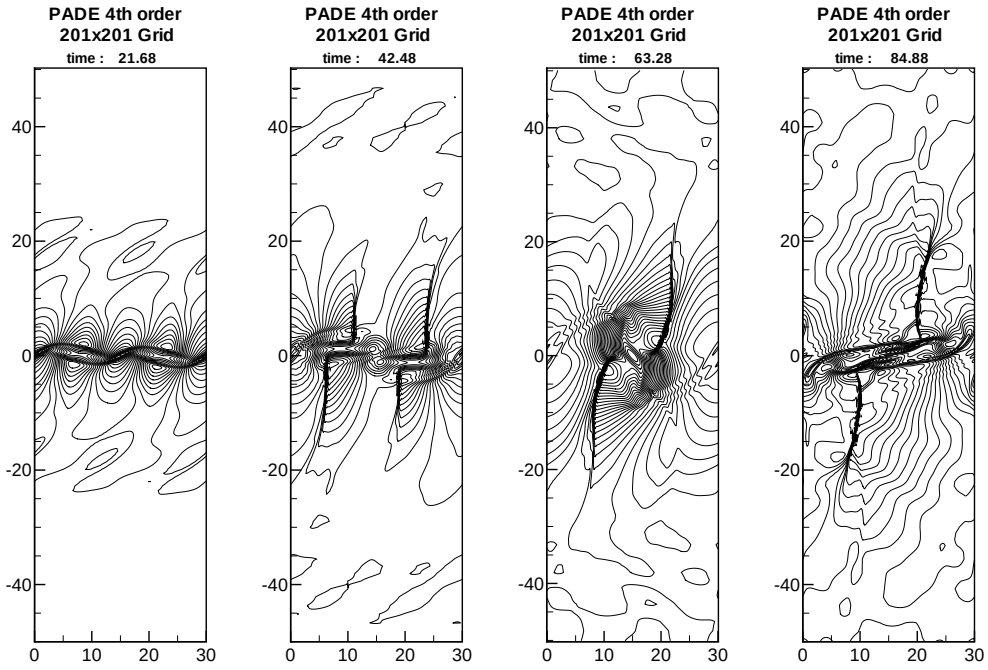

Figure 1: Four stages of vortex pairing at times t= 21.68, 42.48, 63.28, 84.88, showing the temperature contours for a 201x201 Grid using the 4^{th}-order pade scheme with a 6^{th}-order filter.

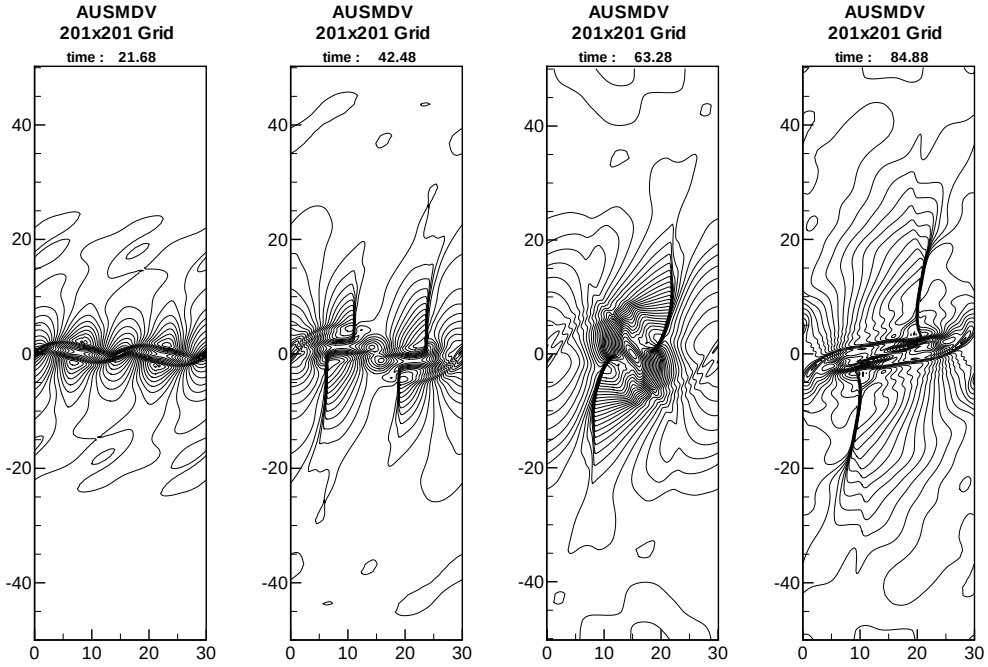

Figure 2: Four stages of vortex pairing at times t= 21.68, 42.48, 63.28, 84.88, showing the temperature contours for a 201x201 Grid using the 2^{nd}-order AUSMDV upwind scheme.

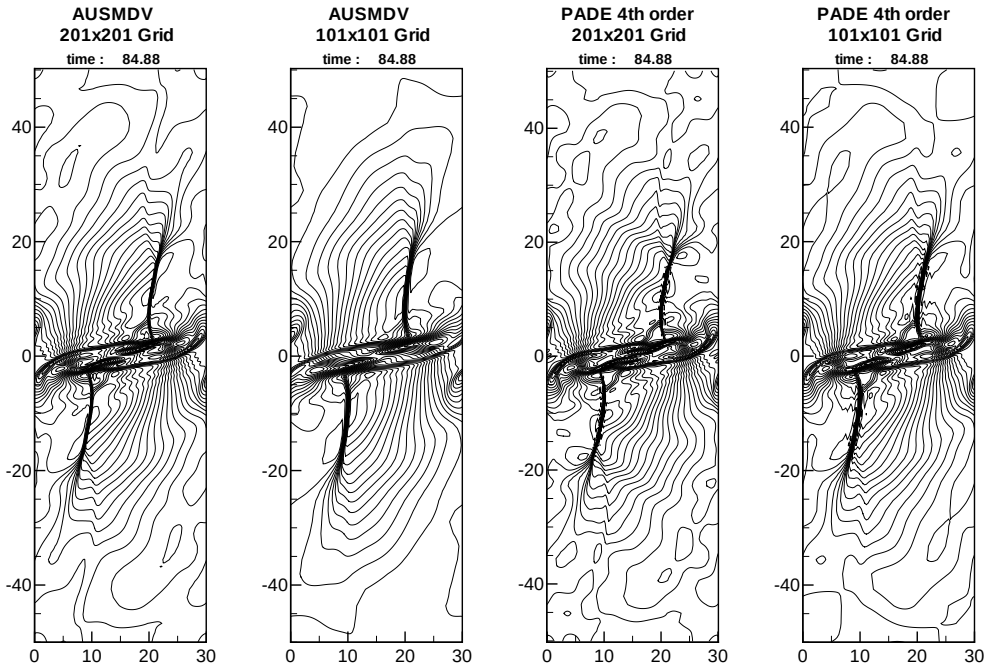

Figure 3: Impact of different schemes on the resolution of the vortex-structures resulting from the vortex pairing at t=84.88, illustrated by temperature contours for two grid densities and two numerical schemes.

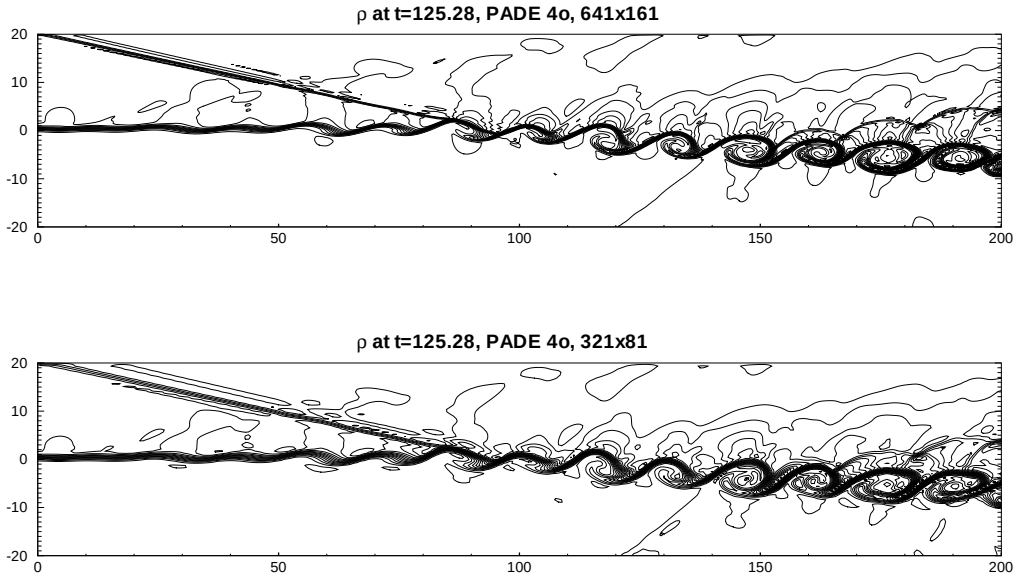

Figure 4: Comparison of density contours for the shock-shear-layer test case at t=125.28 calculated on two grids by the 4^{th}-order pade scheme with a 6^{th}-order filter.

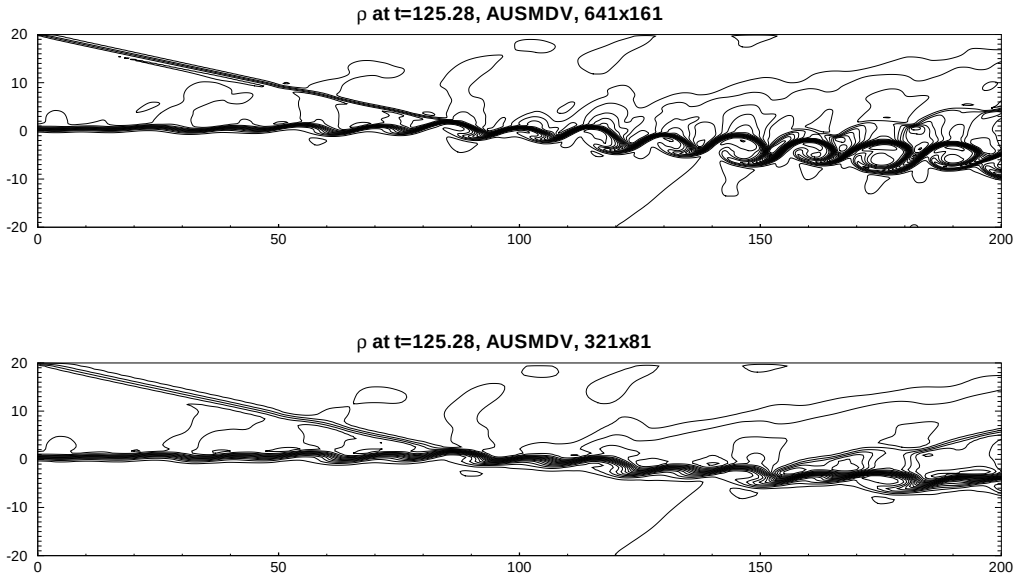

Figure 5: Comparison of density contours for the shock-shear-layer test case at t=125.28 calculated on two grids by the 2^{nd}-order AUSMDV upwind scheme.

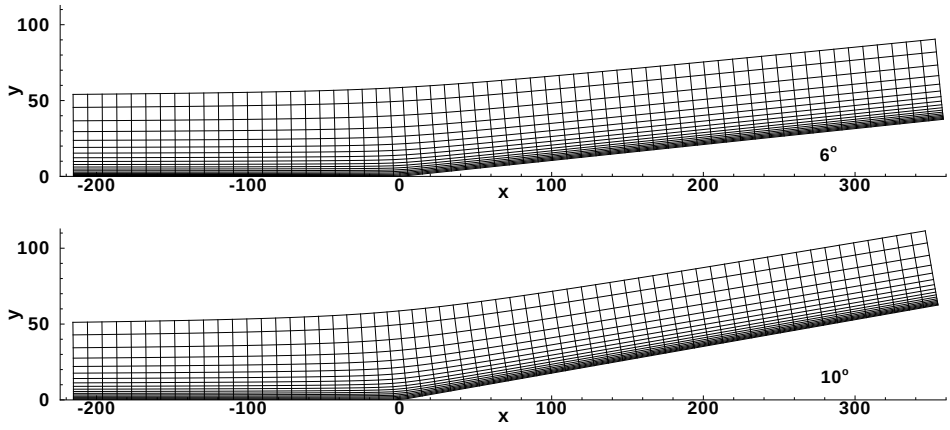

Figure 6: Examples for ramp-grids in the physical space at different ramp angles, scaled by the inflow-displacement thickness δ_{in}. Every 10^{th} grid point shown.

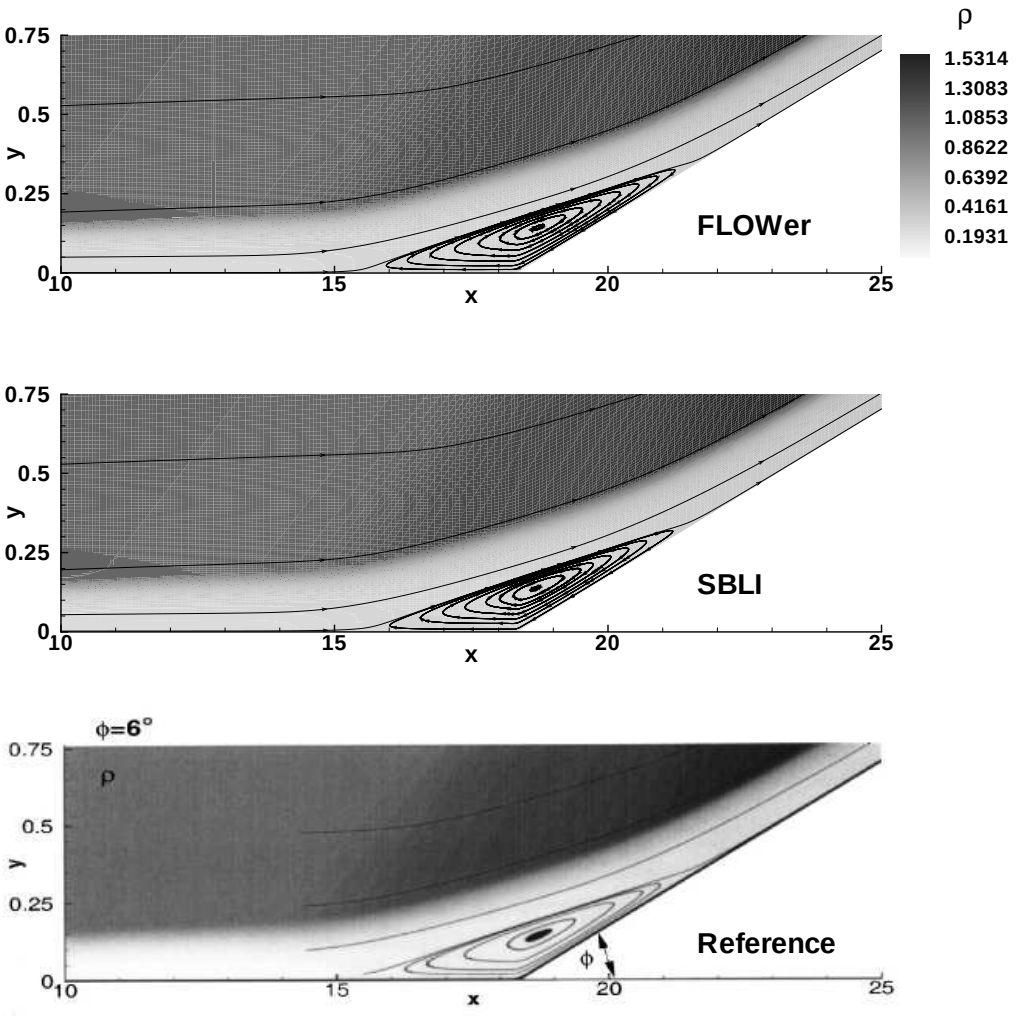

Figure 7: Density field and streamtraces for 6° ramp at $Re_{\delta,in}$=6843. Upper figure: Flower result, lower figure and general scaling taken for comparison from Pagella [5].

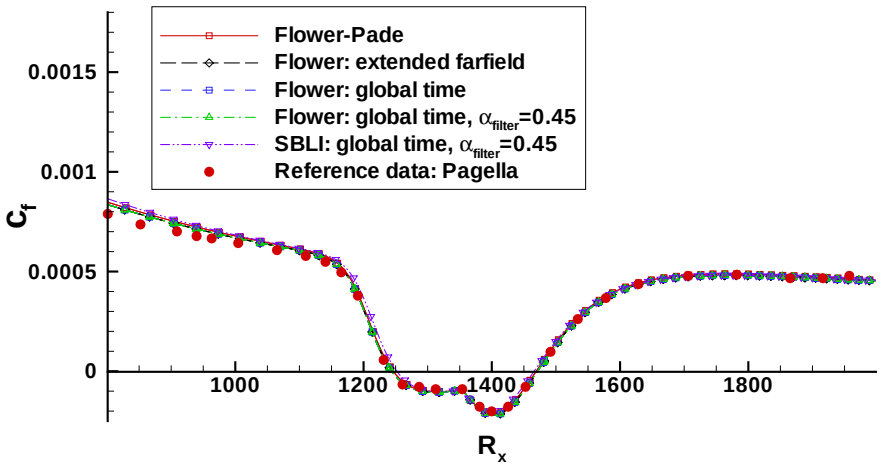

Figure 8: Skin friction distribution for 6° ramp at $Re_{\delta,in}$=6843: c_f versusus local Reynolds number R_x. Comparison of FLOWer- and SBLI results by using different parameter variations (every 10th grid-point shown) with data from Pagella [5].

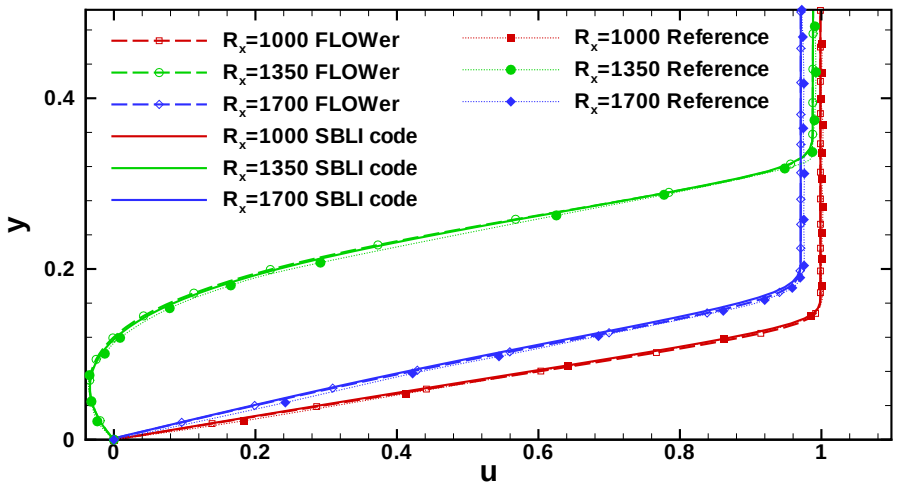

Figure 9: Streamwise velocity components for 6° ramp at $Re_{\delta,in}$=6843 at three different locations. Comparison of FLOWer- and SBLI results with profiles (and scaling of y coordinate) taken from Pagella [5]

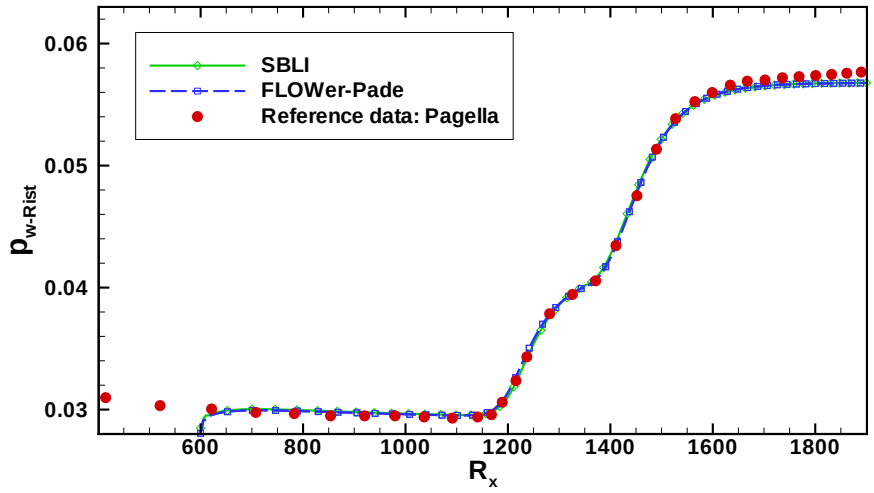

Figure 10: Wall pressue distribution for 6° ramp at $Re_{\delta,in}$=6843 versusus local Reynolds number R_x. Comparison of FLOWer- and SBLI results with pressure distribution taken from Pagella [5]

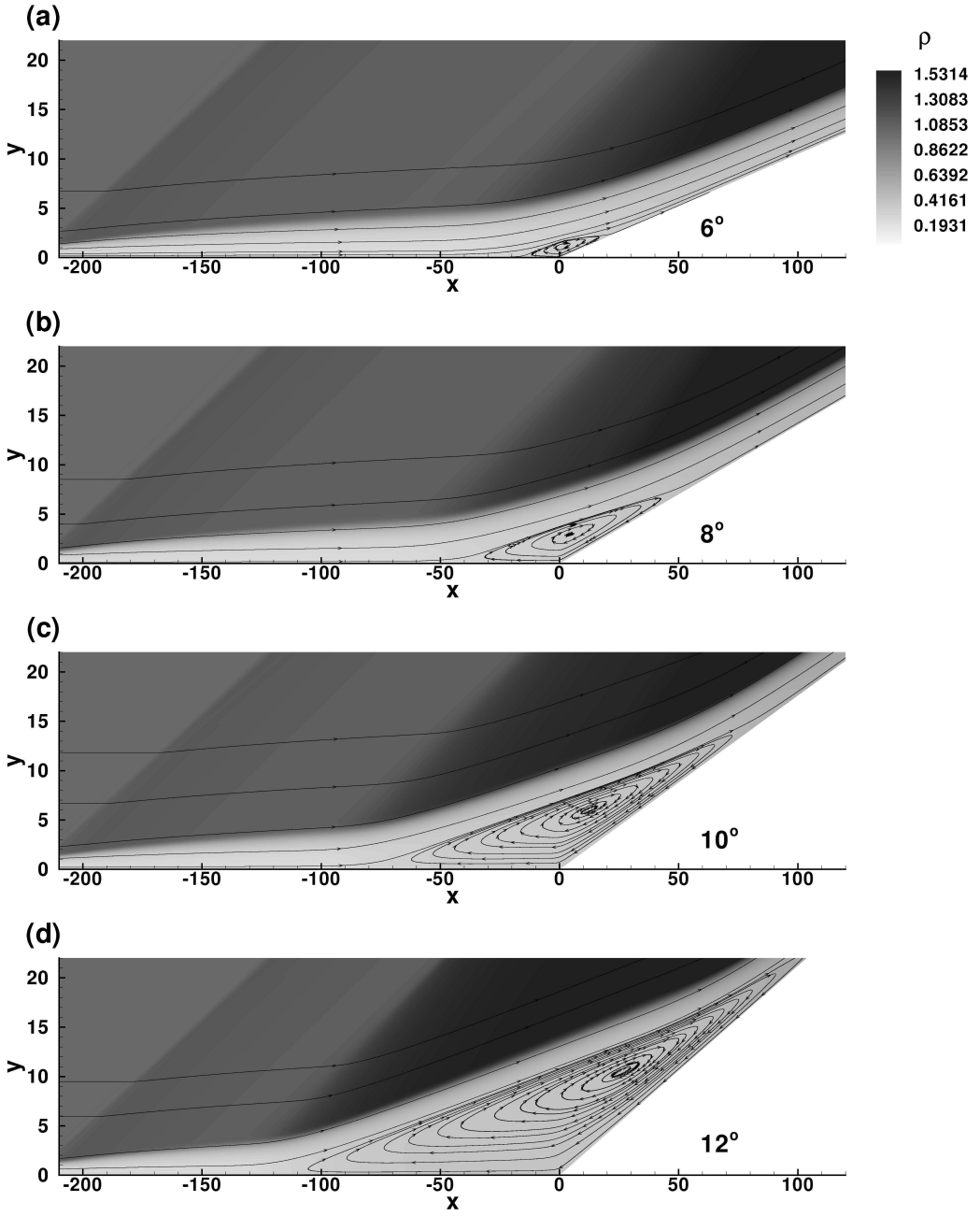

Figure 11: Density distribution and streamlines for ramp angles of $6°, 8°, 10°$ and $12°$ at $Re_{\delta,in}$=6843.

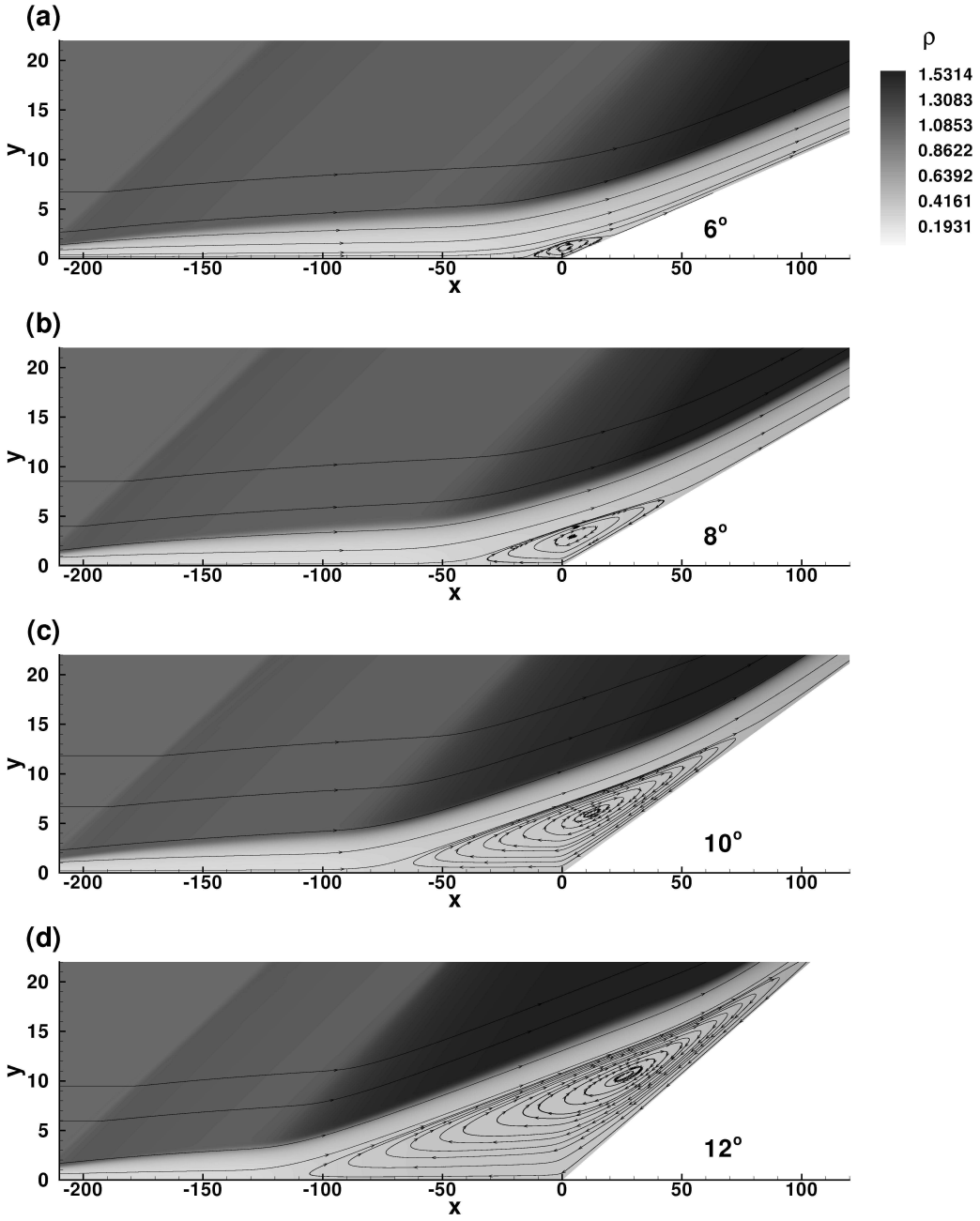

Figure 12: Density distribution and streamlines for ramp angles of $6°, 8°, 10°$ and $12°$ at $Re_{\delta,in}$=3422.

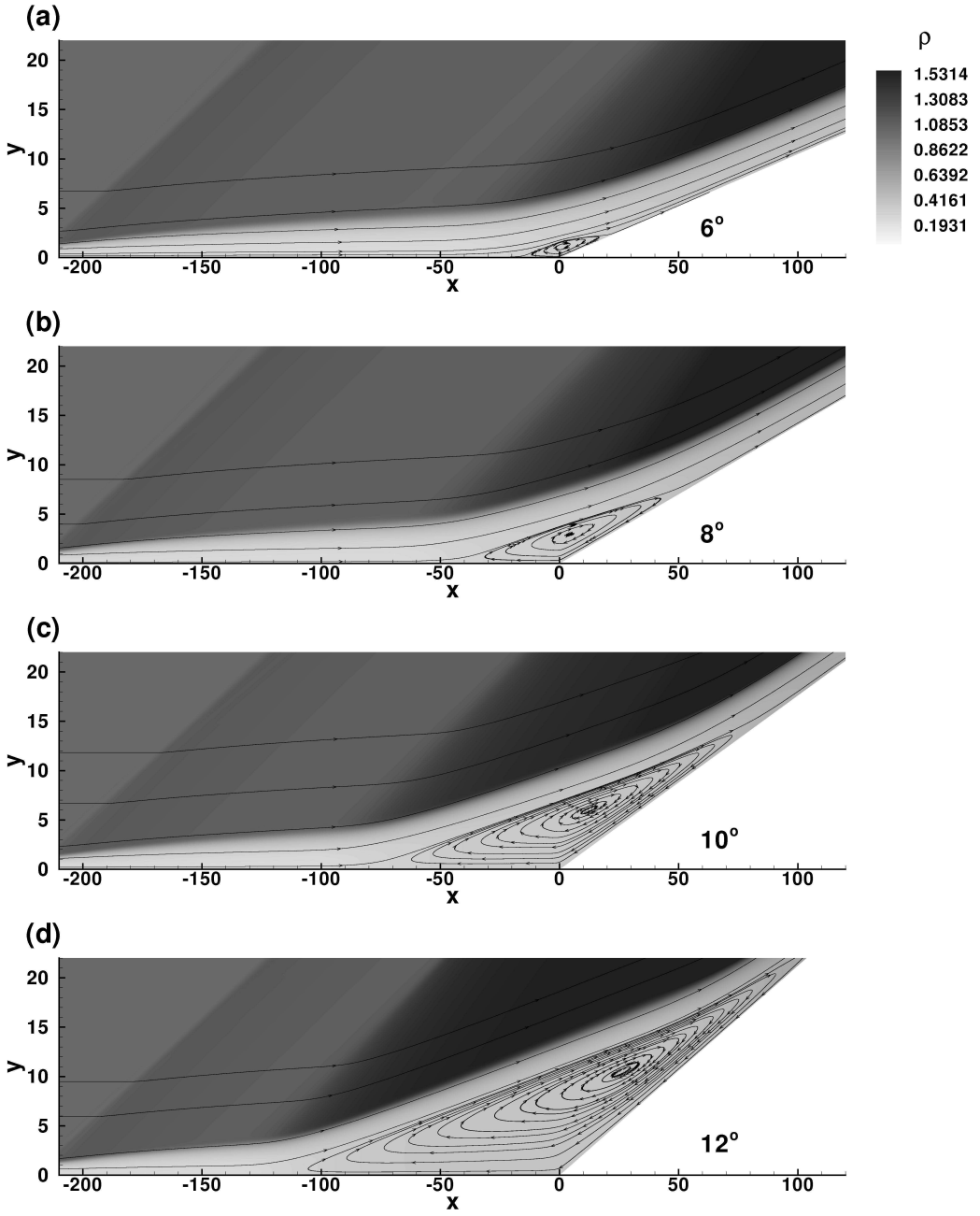

Figure 13: Density distribution and streamlines for ramp angles of $6°, 8°, 10°$ and $12°$ at $Re_{\delta,in}$=1711.

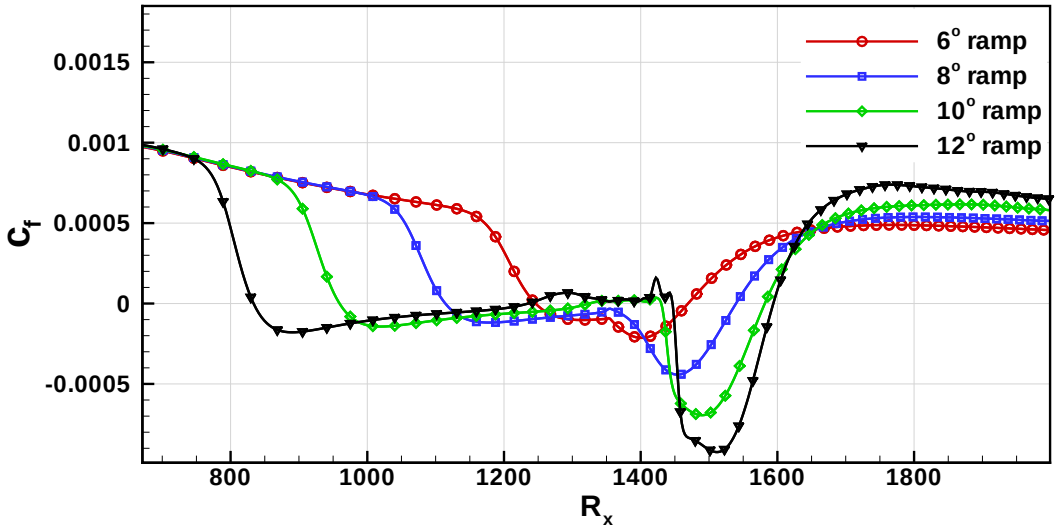

Figure 14: Shear stress distribution for ramp angles of $6°, 8°, 10°$ and $12°$ at $Re_{\delta,in}$=6843.

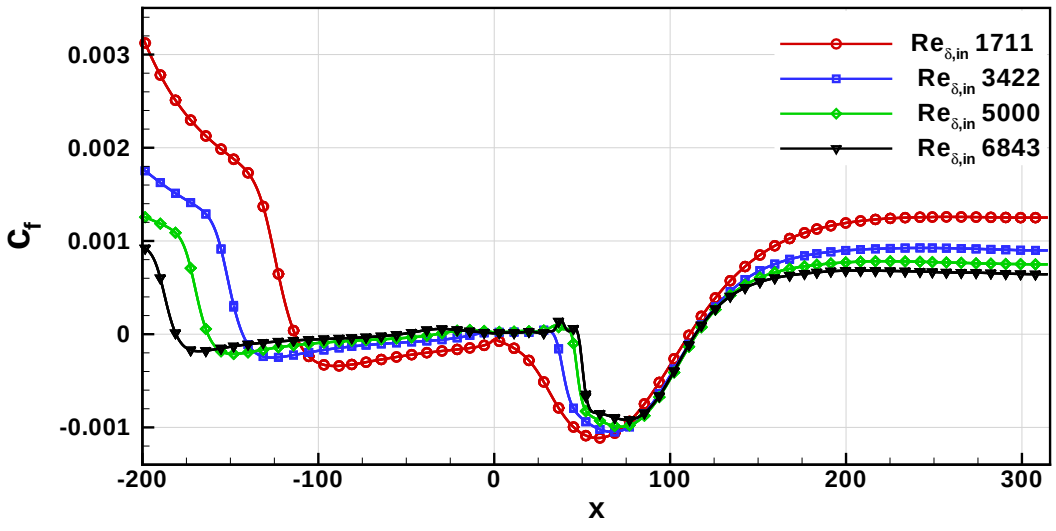

Figure 15: Shear stress distribution for a ramp angle of $12°$ at different $Re_{\delta,in}$ values.

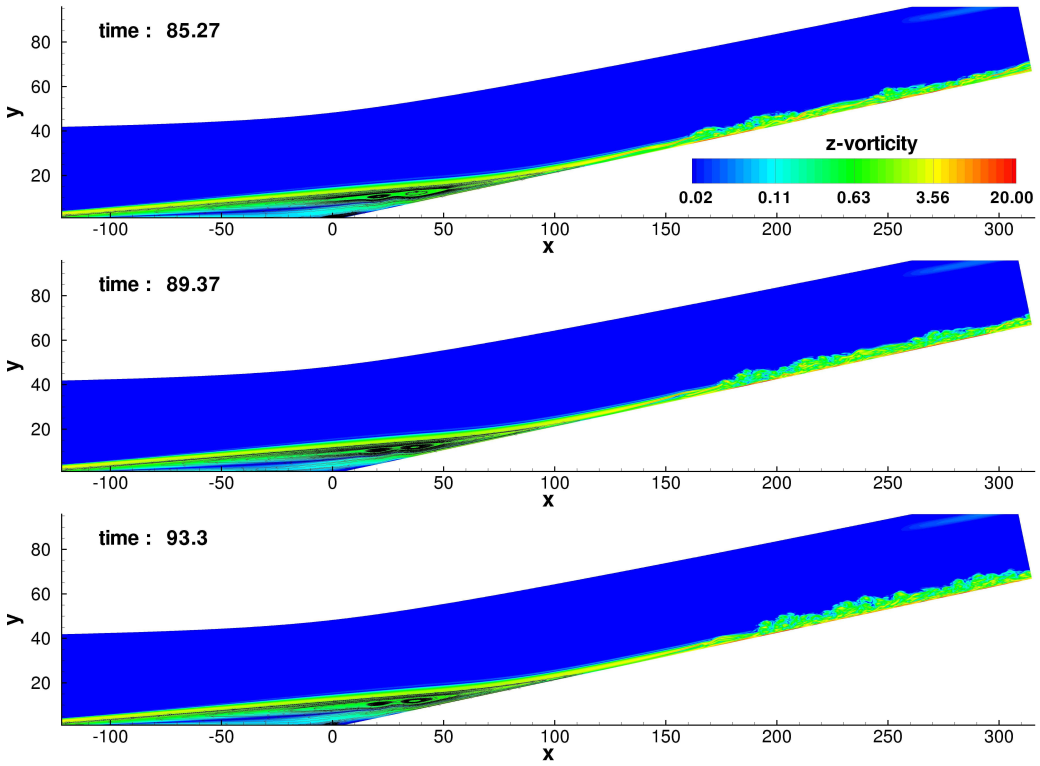

Figure 16: Spanwise vorticity component in the field for a 12° ramp at $Re_{\delta,in} = 3422$ at four successive time instants.

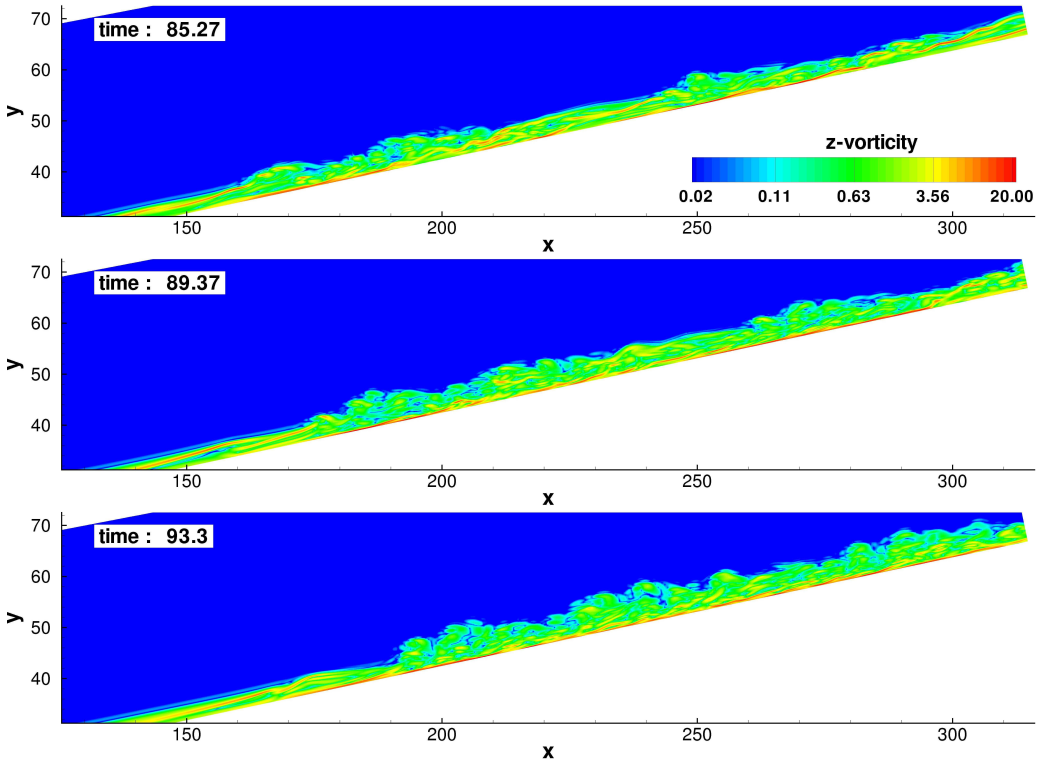

Figure 17: Spanwise vorticity component in the field for a 12° ramp at $Re_{\delta,in} = 3422$ at four successive time instants. cutout behind re-attachment.

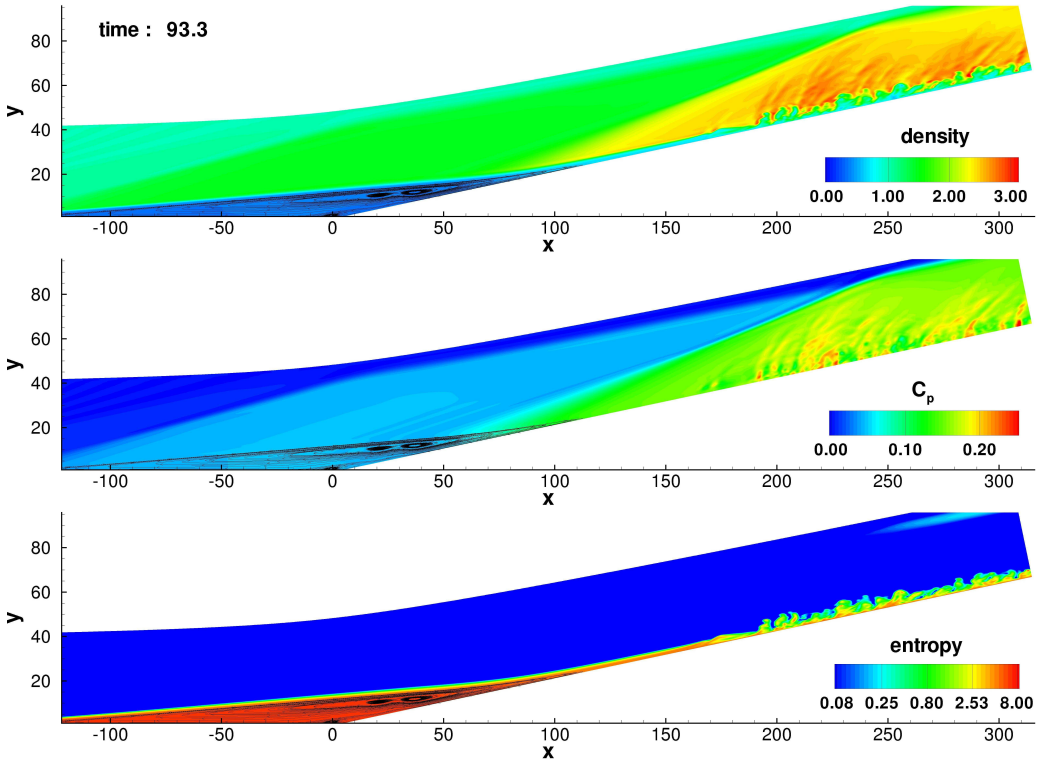

Figure 18: Density, pressure and entropy distribution for a 12° ramp at $Re_{\delta,in} = 3422$.

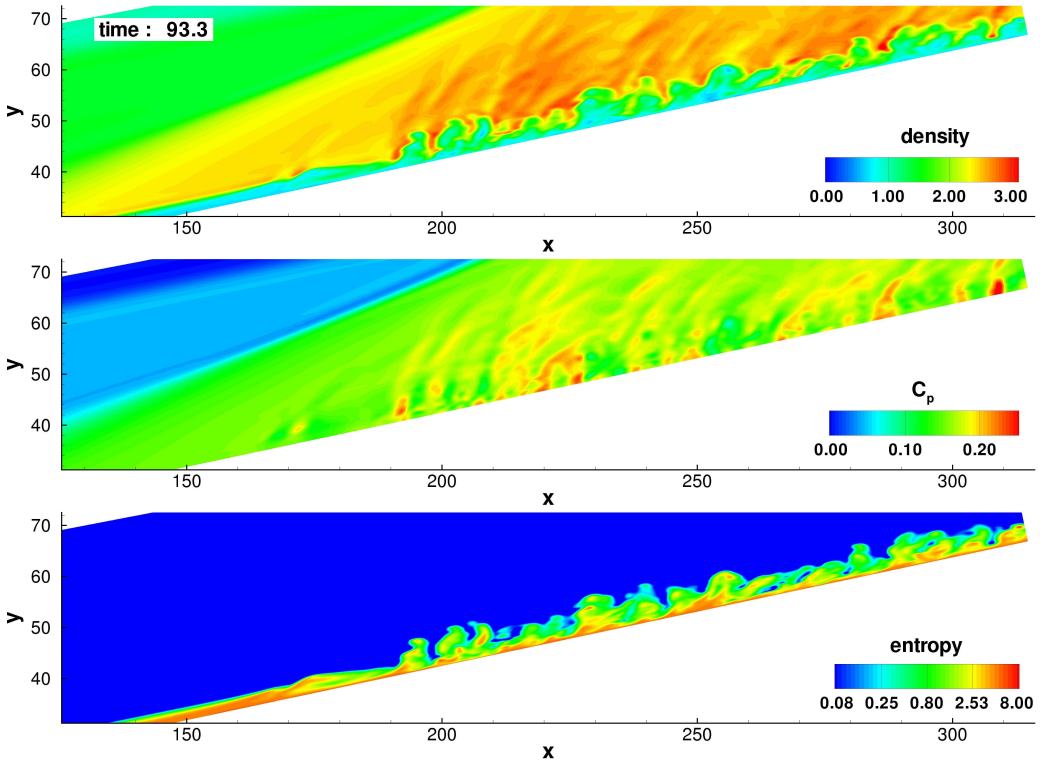

Figure 19: Density, pressure and entropy distribution for a 12° ramp at $Re_{\delta,in} = 3422$. cutout behind re-attachment.

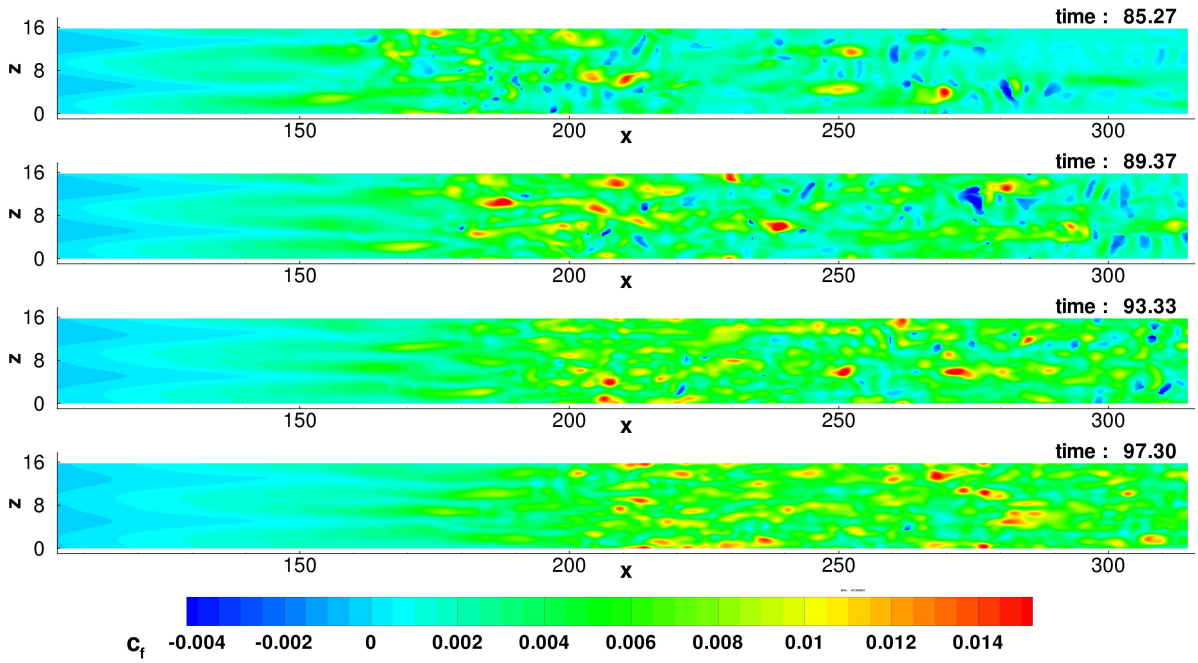

Figure 20: Wall shear stress distribution for a 12° ramp with a spanwise extent of 16 at $Re_{\delta,in} = 3422$ at four successive time instants.

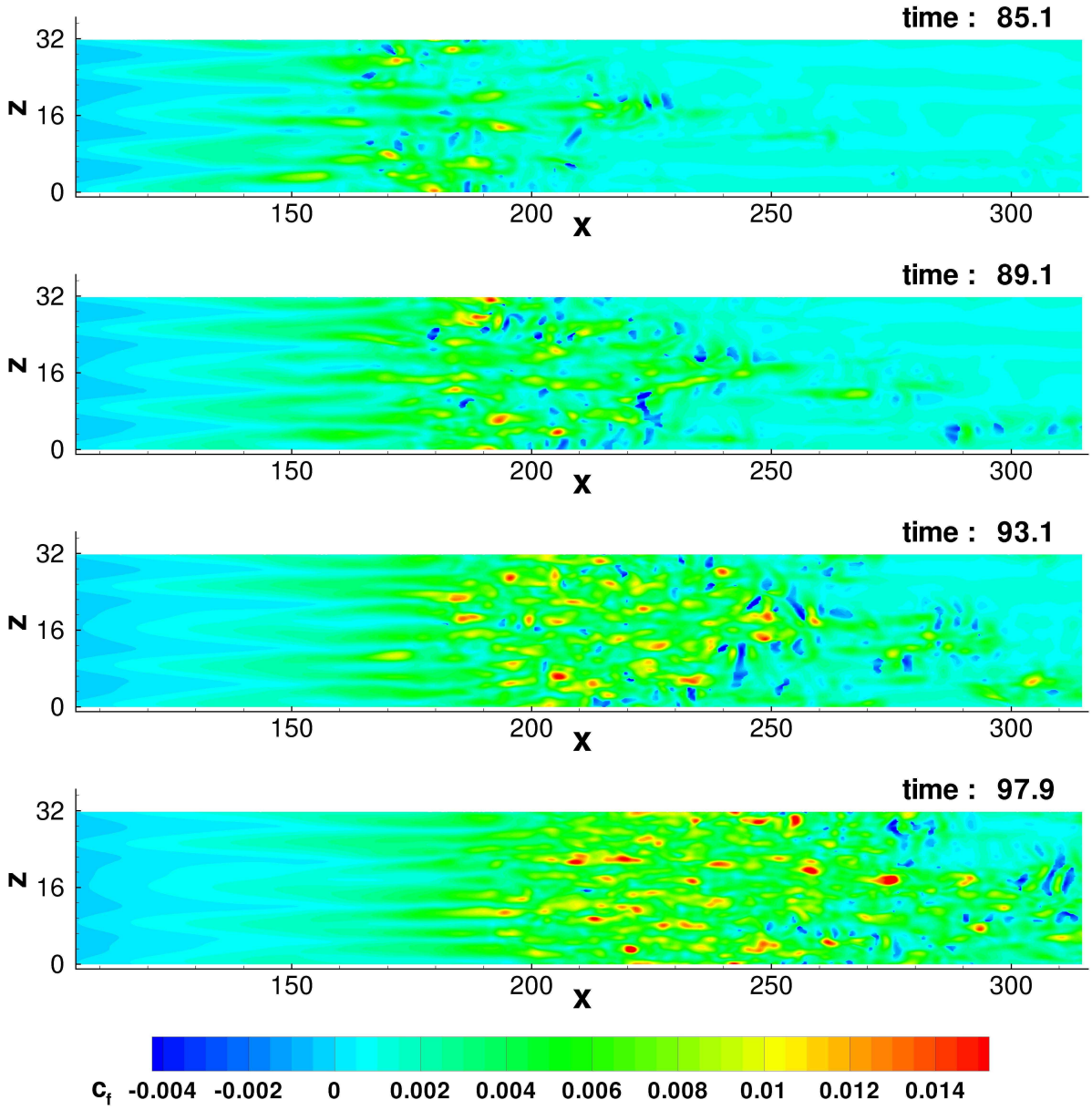

Figure 21: Wall shear stress distribution for a 12° ramp with a spanwise extent of 32 at $Re_{\delta,in} = 3422$ at four successive time instants.

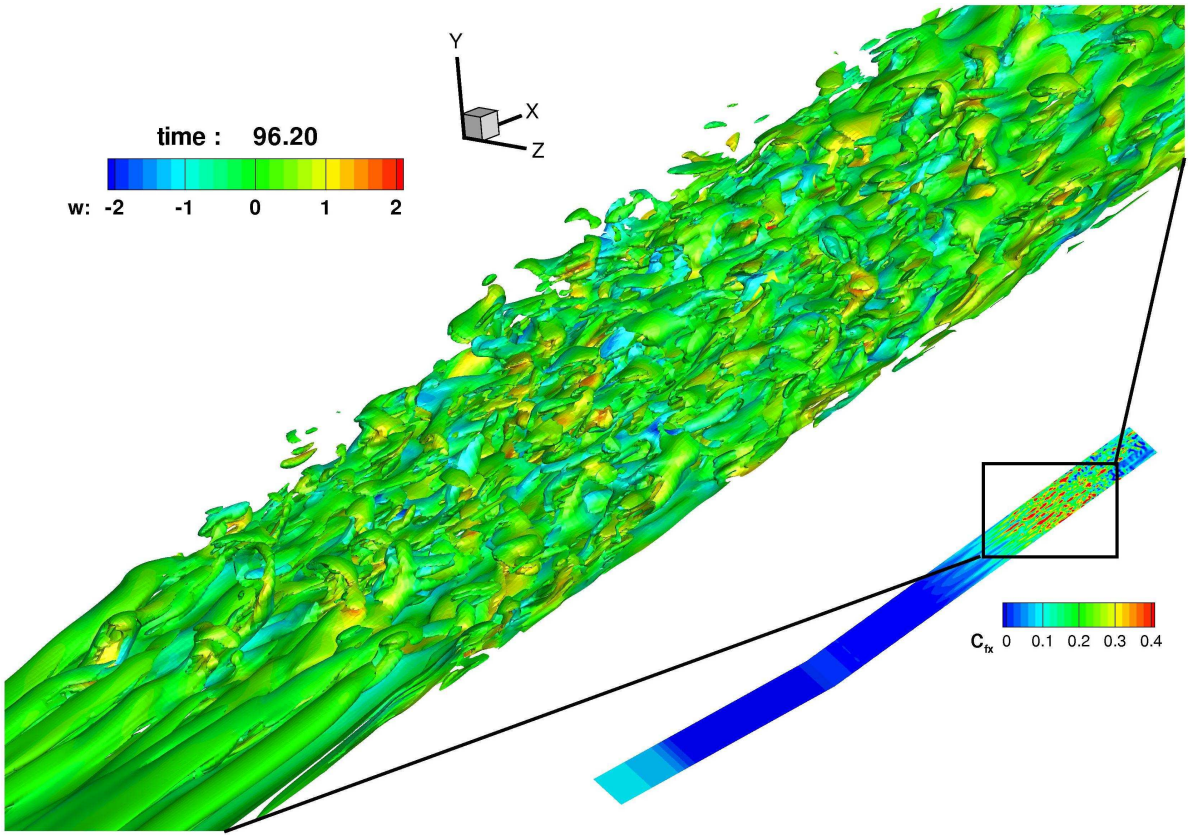

Figure 22: Iso-vorticity distribution coloured by spanwise velocity component for a 12° ramp with a spanwise extent of 32 at $Re_{\delta,in} = 3422$ at t=96.2 dimensionless time units. Inset with contours of the streamwise component of the wall shear stress.

IB 124-2009/9

Calculations of Shock-Boundary Layer Interaction for a Supersonic Ramp Flow by DNS, Using a Fourth order Finite Difference Method

H. Lüdeke, N.D. Sandham

Verteiler:

Institut für Aerodynamik und Strömungstechnik, BS	1	Exemplar
Institut für Aerodynamik und Strömungstechnik, GÖ	1	Exemplar
Verfasser ..... je	2	Exemplare
Prof. Dr.-Ing. habil. C. Rossow	1	Exemplar
Prof. Dr.-Ing. A. Dillmann	1	Exemplar
Dr.-Ing. J.M.A. Longo	1	Exemplar
Dr.-Ing. K. Hannemann	1	Exemplar
ESA Bibliothek	2	Exemplare
Deutsche Bibliothek Frankfurt am Main	2	Exemplare
Niedersächsische Landesbibliothek Hannover	1	Exemplar
Technische Informationsbibliothek Hannover	1	Exemplar
Zentralbibliothek	2	Exemplare
Reserve	5	Exemplare
	23	Exemplare